Synthesis, Crystal Structure, and Characterization of $Na_2SrV_4O_{12}$: A Low-firing Dielectric Vanadate

Chunchun Li[1, 2*], Yingzhi Meng[2], Hongping Hou[1], Amei Zhang[1], Jibran Khaliq[3], Na Liao[1], Caixia Fu[1], Laijun Liu[2], Hongliang Du[1]

[1]*College of Engineering, Xi'an International University, Xi'an 710077, China*

[2] *Guangxi University key laboratory of non-ferrous metal oxide electronic functional materials and devices, College of Material Science and Engineering, Guilin University of Technology, Guilin, 541004, China*

[3]*Department of Mechanical and Construction Engineering, Faculty of Engineering and Environment, Northumbria University at Newcastle, NE1 8ST, UK*

Abstract

In this work, cyclotetravanadate $Na_2SrV_4O_{12}$ was synthesized at a relatively low sintering temperature of ~ 500 °C using a solid-state reaction method. X-ray diffraction and transmission electron microscope characterization featured a tetragonal structure that was built by a 3D frame of isolated tetracyclic $(V_4O_{12})^{4-}$. Dielectric measurements demonstrated strong dependence on frequency and temperature. A low relative permittivity of $\varepsilon_r \sim 8 \pm 0.2$ and a dielectric (loss $\tan\delta$) $\sim 0.4 \pm 0.01$ was achieved at a frequency of 10 kHz and room temperature. *ac* impedance and conductivity analysis revealed a thermally activated migration behavior of charge carriers with a short-range hopping feature. XPS analysis validated the existence of oxygen vacancy and reduction in vanadium (from V^{5+} to V^{4+}), which gave rise to charged lattice defects. The migration or hopping of such charged defects

* Authors to whom correspondence should be addressed: lichunchun2003@126.com;

This is the author manuscript accepted for publication and has undergone full peer review but has not been through the copyediting, typesetting, pagination and proofreading process, which may lead to differences between this version and the Version of Record. Please cite this article as doi: 10.1111/jace.19019.

was responsible for the observed electrical behaviors. Owing to the simple composition, inexpensive raw materials, and low density (2.99 g/cm^3) make $Na_2SrV_4O_{12}$ ceramic a potential candidate for lightweight devices and in photocatalytic degradation and all-solid-state ion batteries.

Keywords: Ceramics; Dielectric properties; Low-temperature firing; Vanadate

1. Introduction

Metal vanadates have been widely applied as the matrix in fluorescence and laser materials, and recently showed promising application potential in photocatalyst and lithium-ion batteries due to their low dielectric permittivity and low loss [1-5]. Compared to silicates, crystalline vanadates possess versatile structural chemistry stemming from the various extension of vanadium-oxygen polyhedra [6-9]. Depending on the manner of polymerization, diverse structural configurations are formed in vanadates, including chains, sheets, and three-dimensional blocks [10-13]. Among them, a rare cyclic structure configuration, which was built by an isolated tetracyclic unit [V_4O_{12}], has been specialized. Till now, such materials have been rarely reported and are mainly based on a general formula $M_2M'(XO_3)_4$, e.g., $Na_2Sr(VO_3)_4$, $CaY_2(GeO_3)_4$[7, 14].

In our previous work, $Na_2CaV_4O_{12}$, as a representative cyclic compound was characterized in terms of solid-state preparation, phase transition, dielectric, and ionic properties. A phase transition was identified at based on various X-ray diffraction and dielectric behaviors. The ionic conductivity of $Na_2CaV_4O_{12}$ was observed to be strongly

correlated to the phase structure. It is reported that the coordination condition for alkaline-earth metals in the cyclic $M_2M'(XO_3)_4$ varies from a square antiprism to a prism [8, 15]. Such crystal evolution was expected to induce various dielectric and conductivity behaviors

which were effectively influenced by the polyhedral deformation, the ionic radii and the polarizability of central cations. Especially for the cyclic $M_2M'(XO_3)_4$ structure, the dielectric properties were mainly influenced by the coordination condition for alkaline-earth metals. Moreover, the ultra-low sintering temperature (500 °C) and lightweight make it of great potential in the industrialization of ceramics from the perspective of reducing energy consumption and costs.

Motived by the interesting structural and physical properties, it is worthwhile to exploit novel dielectric materials of this family. Considering the same valence and similar cation size of Sr^{2+} to Ca^{2+}, $Na_2SrV_4O_{12}$ was fabricated in this work and the phase formation, crystal structure, and dielectric properties were characterized in detail. Combined ac impedance spectrum and complex modulus plots were employed to unveil the electrical conduction mechanism.

2. Experimental

Preparation of $Na_2SrV_4O_{12}$ ceramics: Ceramic powders were prepared by the traditional solid-state reaction using stoichiometric ratios of Na_2CO_3 (99.9%), $SrCO_3$ (99.9%), and V_2O_5 (99.99%) as raw materials. The powders were mixed by ball-milling with

alcohol as a grinding medium for 6 h. The calcination was conducted in a temperature range of 100-500 ℃ for 4 h to study the phase formation. After calcination, a second ball-milling for 6 h was carried out mixed with PVA (5 wt.% solutions) as binders. The mixed granules were pressed into pellets with a diameter of 10 mm and thickness of 1-2 mm under a pressure of 80 MPa. The pellets were sintered at 550 °C for 6 h in air.

Characterization: Phase formation was analyzed using differential thermal analysis (DTA) and thermogravimetry (TG) with a PerkinElmer STA8000 from 25 to 600 °C. Phase purity of the fabricated ceramics and constituents of the calcined powders were identified by XRD (X'Pert PRO, PANalytical, Netherlands). Microstructures were analyzed through SEM (JSM-6380, Japan) and TEM (JEM-2100F, Japan). Dielectric properties were measured by a precision impedance analyzer (Agilent 4294A, USA) over a broad frequency (40 -10^7 Hz) and temperature range (25-450 ºC). The temperature was controlled using a hand-made furnace. Before dielectric measurements, silver electrodes were painted on both sides of the sintered pellets.

3. Results and discussion

To confirm the chemical reaction and associated temperatures of $Na_2SrV_4O_{12}$, thermal analysis was carried out on the uncalcined stoichiometric mixtures. A total mass loss of ~ 15% was shown over the detectable temperature range from room temperature to 600 ºC (Fig. 1a). The decomposition of precursors carbonates (Na_2CO_3 and $SrCO_3$) releases carbon dioxide which was responsible for the mass loss which is in accordance with the theoretical

calculation for CO_2 release from the raw materials (14.3%). A sharp drop in mass at 493 ºC was a result of chemical reaction to form the targeted $Na_2SrV_4O_{12}$ phase along with a broad exothermic peak. Another broad endothermic peak with no mass loss was detected around 550 ºC, which could be related to the densification of the $Na_2SrV_4O_{12}$ phase.

Fig. 1 shows XRD pattern of the $Na_2SrV_4O_{12}$ powders synthesized at a broad temperature range (120-500 ºC). In the lower temperature range (120-300 °C) the main phases were $SrCO_3$ (PDF: 005-0418) and $NaVO_3$ (PDF: 032-1997), which indicated that such low heating temperatures were insufficient for the chemical reaction or decomposition of $SrCO_3$.With increasing temperatures, the diffraction peaks from $NaVO_3$ became intense, which accounted for the reaction between Na_2CO_3 and V_2O_5. This result corresponds to the first DSC curve with no mass loss as shown in Fig.1a. On increasing the temperature in the range of 300-450 °C, $Sr_2V_2O_7$ (PDF: 071-1593) and $Na_{10}V_{24}O_{64}$ (PDF: 019-1257) appeared in addition to the $NaVO_3$ phase. Upon increasing the temperature to 500 °C, the XRD pattern matched well with the standard card of $Na_2SrV_4O_{12}$ (PDF: 00-052-1891) with no second phase detected. This result indicated that the objective $Na_2SrV_4O_{12}$ phase can be purified at 500 °C.

Rietveld refinement was utilized to confirm the phase purity and reveal the crystal structure of $Na_2SrV_4O_{12}$. A tetragonal structural model based on P4/nbm was established. As shown in Fig. 2a, a good fit between the calculated and observed profiles results in reliable factors (R_{wp} = 6.87%, Rp = 4.46%, and χ^2 = 2.13, as shown in Table 1). The crystal structure of $Na_2SrV_4O_{12}$ could be described as a 3D frame of isolated cyclic $(V_4O_{12})^{4-}$ which is built of

four corner-shared (VO_4) tetrahedra (in the inset of Fig. 2a). The as-sintered ceramic exhibited dense microstructure of closely packed grains with an average grain size of ~ 8 μm (Fig. 2b), which conforms to the high relative density (95.6%). TEM analysis of $Na_2SrV_4O_{12}$ ceramics with a $[\bar{1}\bar{1}4]$ zone axis provided valid evidence for the tetragonal structure, as shown in the diffraction pattern in Fig. 2(c). The lattice parameter of ~0.276 nm along the $[\bar{2}21]$ direction is illustrated in Fig. 2(d).

To investigate the dielectric properties of $Na_2SrV_4O_{12}$ ceramics, variations in relative permittivity (ε_r) and dielectric loss tangent ($\tan\delta$) were measured as a function of frequency and temperature. As shown in Fig. 3a, typical frequency dependence was displayed, especially at the low-frequency range (as marked by the light-blue shadow), which led to a relatively smooth change over 10 kHz. Similar frequency dispersion was also observed in the temperature-dependence dielectric behavior (Fig. 3b). These dielectric behaviors can be explained by the existence of some slow polarization dipoles, such as space charge polarization, which disappear at high frequencies but could be triggered at high temperatures. [16, 17]. In addition, the temperature curves (Fig. 3b) did not show any abnormal dielectric peaks, which indicated no phase transition took place in the temperature range tested. This is different from the previously reported $Na_2CaV_4O_{12}$ counterpart, exhibiting a dielectric anomaly at 515 °C[6]. It should be noted that in the temperature range of 25-300 °C, both ε_r and $\tan\delta$ remained essentially constant, demonstrating thermal stability. A room-temperature relative permittivity $\varepsilon_r \sim 8$ at 10 kHz along with a high dielectric loss ($\tan\delta \sim 0.4$) were obtained.

To probe the origin of high dielectric loss, complex impedance spectroscopy was employed over a broad frequency (40-10^6 Hz) and temperature (643-733K) range. As shown in Fig. 4a-c, one electrical response was active in the measured frequency and temperature region, which was featured by only one relaxation behavior in the Z''-f curves and one semicircular arc in the Z''-Z' curves. To further reveal the relaxation process, the imaginary impedance was normalized, from which the characteristic relaxation frequency (f) could be obtained. The temperature variation in the f value can be expressed by the Arrhenius formula[18-20]:

$$f = f_0 \exp(-\frac{E_a}{K_B T}) \quad (1)$$

Where f_0 is the pre-exponential factor, E_a represents relaxation activation energy, K_B refers to the Boltzmann constant, and T is kelvin temperature. As shown in Fig. 4c, an apparent line relationship between Lnf and $1/T$ exists and via linear fitting, the relaxation activation energy E_a (1.03 eV) was obtained. According to the literature, it is speculated that the relaxation process of $Na_2SrV_4O_{12}$ ceramic samples might be related to the migration of charge carriers such as oxygen vacancies [21, 22].

To gain an insight into the migration mechanism of the charge carriers, modulus spectroscopy of $Na_2SrV_4O_{12}$ was carried out to supplement the impedance analysis. Fig. 4d shows the variation in the imaginary part of modulus (M'') as a function of frequency at some fixed temperatures. Like the impedance (Z''), strong frequency dependence was demonstrated, which was characterized by a low-frequency relatively smooth region and a

rapid increase in the high-frequency region. Such a variation resulted in a series of relaxation peaks which shifted towards the higher-frequency side with an increase in temperature. It is well known that the modulus spectrum below the relaxation peak frequency is partly due to the long-range distance of the carrier in the crystal, while the part above the relaxation peak frequency is caused by short-range mobility [23-25]. The relaxation of the modulus spectrum can be expressed by the following Fourier transformation equation:

$$M^* = [1 - \int_0^\infty \exp(-wt)(-\frac{\mathrm{d}\phi}{\mathrm{d}t}\frac{\mathrm{d}\phi}{\mathrm{d}t})] \quad (2)$$

Where $\varphi(t)$ is a time constant related to the frequency of change of the alternating electric field and can be expressed as:

$$\varphi(\mathrm{t}) = \exp\left[-t / \tau_m{}^{\beta}\right] \quad (3)$$

Here, $\varphi(t)$ is the relaxation time of the conductivity, β ($0 < \beta \leq 1$) is a parameter indicating the degree of deviation of relaxation from the ideal Debye relaxation. Otherwise, Bergman proposed a simpler KWW formula as follows:

$$M''=M''_{\max} / \left\{(1-\beta) + \frac{\beta}{1+\beta}\left[\beta(w_{\max} / w) + (w_{\max} / w)^{\beta}\right]\right\} \quad (4)$$

Where M''_{max} is the maximum value of the imaginary modulus (M''), w_{max} is corresponding to the frequency of the M''_{max}. The β values obtained by fitting are shown in Fig. 4e as a function of temperature. A continuous increase in β value was observed with increasing temperature. This indicated that the number of carriers that contribute to the

conductivity increases with temperature. Additionally, the separate peaks for the normalized Z''/Z''_{max} and M''/M''_{max} at 653 K, as illustrated in Fig. 4f, indicated the migration of charge carriers in the present $Na_2SrV_4O_{12}$ ceramics is short-range[24].

The frequency dependence of *ac* conductivity (σ_{ac}) at some selected temperatures is shown in Fig. 5a. The ac conductivity is independent of frequency at a low-frequency range (< 10^4 Hz), and strong frequency dependence was demonstrated when the frequency exceeded 10^5 Hz. According to the universal dielectric response, the *ac* conductivity is fitted:

$$\sigma_{ac}=\sigma_{dc}+\sigma_0 f^s \quad (5)$$

Where the σ_{ac} is the *ac* conductivity, σ_{dc} is the *dc* conductivity, σ_0 is a constant, f is the frequency, and s ($0< s \leq 1$) is the pre-exponential factor. By fitting, the *dc* conductivity can be obtained and is shown in Fig. 5b as a function of temperature. As the temperature rises, the *dc* conductivity showed an upward trend, suggesting the semiconductor nature of $Na_2SrV_4O_{12}$. Additionally, the relationship between the fitted dc conductivity and the temperature was studied via the Arrhenius formula:

$$\sigma_{dc}=\sigma_0 \exp(-\frac{E_{con}}{K_B T}) \quad (6)$$

where σ_{dc} is the dc conductivity; σ_0 is the pre-exponential factor; E_{con} is the activation energy of *dc* conductivity. A linear correlation existed between $\ln\sigma_{dc}$ and $1/T$, resulting in a slope of 0.822 eV (E_{con}). This result further indicates that the electrical behavior of $Na_2SrV_4O_{12}$ is attributed to the thermally activated charge carriers.

XPS spectra on Na, Sr, V, and O elements of $Na_2SrV_4O_{12}$ are shown in Fig. 6. By fitting via the Gaussian sub-peaks, the oxide state of Na and Sr was confirmed as +1 and +2, whereas partial reduction of V^{5+} to V^{4+} was also observed. The V $2p_{3/2}$ and V $2p_{1/2}$ located at 516.8 eV and 524.4 eV with a spin-orbit splitting of 7.6 eV were assigned to V^{5+}. Whereas those located at 516 eV and 522.5 eV were assigned to V^{4+}, which is consistent with the previous report [7]. For the O-1s XPS spectrum, the 529.7 eV peak corresponded to the oxygen ion, and the peak at 531.3 eV was assigned to O ions near the oxygen vacancies, which verifies the existence of oxygen vacancies. It has been established that oxygen loss would occur during sintering at elevated temperatures, generating oxygen vacancies [26, 27]. The ionization of oxygen vacancies would release electrons, which could be described based on the defect equations:

$$O_O \longrightarrow V_O + 1/2O_2 \quad (7)$$

$$V_O \longrightarrow V_O^{\bullet} + e' \quad (8)$$

$$V_O^{\bullet} \longrightarrow V_O^{\bullet\bullet} + e' \quad (9)$$

Once the released electrons are captured by the neighboring V^{5+}, reduction to V^{4+} would happen according to the equation:

$$V^{5+} + e' \rightarrow V^{4+} \quad (10)$$

XPS results validated the presence of charge carriers ($V_O^{\bullet\bullet}$, e′, and $(V_V^{4+})'$). The short-range migration or hopping of such carriers gives rise to conductivity, which explains the observed electrical behaviors.

Conclusions

Single-phase $Na_2SrV_4O_{12}$ was successfully synthesized at relatively low temperatures (~ 500 ºC) and the corresponding dense ceramics were fabricated at 550 ºC with a relative density of 95.6%. XRD and TEM confirmed that $Na_2SrV_4O_{12}$ crystallizes into a tetragonal structure with a space group P4/nbm and the crystal structure was built by a 3D frame of isolated tetracyclic $(V_4O_{12})^{4-}$. Dielectric measurements featured a low relative permittivity ε_r ~ 8 with a dielectric loss $\tan\delta$ ~ 0.4 at 10 kHz and at room temperature. *ac* impedance and conductivity analysis revealed a thermally activated migration behavior of charge carriers with a short-range hopping feature. XPS analysis validated the existence of oxygen vacancy and reduction in vanadium (from V^{5+} to V^{4+}), which gave rise to charged lattice defects. The migration or hopping of such charged defects was responsible for the observed electrical behaviors. The ceramic could therefore have the potential for applications in photocatalytic degradation and all-solid-state ion batteries.

Acknowledgments

This work is supported by the Fundamental Research Funds of Shaanxi Key Laboratory of Artificially-Structured Functional Materials and Devices (AFMD-KFJJ-21210) and

Guangxi Key Laboratory Fund of Embedded Technology and Intelligent System (No. 2020-1-6), the Youth Innovation Team of Shaanxi Universities and Scientific Research Program Funded by Shaanxi Provincial Education Department (No. 21JK0869), Natural Science Basic Research Program of Shaanxi (Program No. 2023-JC-YB-441).

References

[1] Xia DW, Gao HP, Li MQ, Gong F, Li M, Transition metal vanadates electrodes in lithium-ion batteries: a holistic review, Energy Stor. Mater. 2021;35:169-191.

[2] Xu XM, Niu CJ, Duan MY, Wang XP, Huang L, Wang JH, Pu LT, Ren WH, Shi CW, Meng JS, Alkaline earth metal vanadates as sodium-ion battery anodes, Nat. Commun. 2017;8(1):1-11.

[3] Dhachapally N, Kalevaru VN, Radnik J, Martin A, Tuning the surface composition of novel metal vanadates and its effect on the catalytic performance, Chem. Commun. 2011;47(29):8394-8396.

[4] Fang GZ, Zhou J, Liang CW, Cai YS, Pan AQ, Tan XP, Tang Y, Liang SQ, General synthesis of three-dimensional alkali metal vanadate aerogels with superior lithium storage properties, J. Mater. Chem. A 2016;4(37):14408-14415.

[5] Vignesh K, Hariharan R, Rajarajan M, Suganthi A, Visible light assisted photocatalytic activity of TiO_2-metal vanadate (M = Sr, Ag and Cd) nanocomposites, Mater. Sci. Semicond. Process. 2013;16(6):1521-1530.

[6] Liu CG, Wu SF, Yin CZ, Xu JG, Xiong Y, Liu LJ, Khaliq J, Li CC, Phase transformation and ionic conductivity mechanism of a low-temperature sintering semiconductor $Na_2CaV_4O_{12}$, J. Alloys Compd. 2021;886(15):161259.

[7] Slobodin B, Surat L, Zubkov V, Tyutyunnik A, Berger I, Kuznetsov M, Perelyaeva L, Shein I, Ivanovskii A, Shulgin B, Structural, luminescence, and electronic properties of the alkaline metal-strontium cyclotetravanadates $M_2Sr(VO_3)_4$, (M = Na, K, Rb, Cs), Phys. Rev. B 2005;72(15):155205.

[8] Zubkov V, Surat L, Tyutyunnik A, Berger I, Tarakina NV, Slobodin B, Kuznetsov M, Denisova T, Zhuravlev N, Perelyaeva L, Structural, vibrational, electronic, and luminescence properties of the cyclotetravanadates $A_2M(VO_3)_4$ (A = Na, Ag; M= Ca, Sr), Phys. Rev. B 2008;77(17):174113.

[9] Mocała K, Ziółkowski J, Polymorphism of the Bivalent Metal Vanadates MeV_2O_6 (Me = Mg, Ca, Mn, Co, Ni, Cu, Zn, Cd), J. Solid State Chem. 1987;69(2):299-311.

[10] Marberger A, Ferri D, Elsener M, Sagar A, Artner C, Schermanz K, Kröcher O, Relationship between structures and activities of supported metal vanadates for the selective catalytic reduction of NO by NH_3, Applied Catalysis B: Environmental 2017;218(5):731-742.

[11] Huang H, Tian T, Pan L, Chen X, Tervoort E, Shih CJ, Niederberger M, Layered metal vanadates with different interlayer cations for high-rate Na-ion storage, J. Mater. Chem. A 2019;7(27):16109-16116.

[12] Kumari S, Junqueira JR, Schuhmann W, Ludwig A, High-Throughput Exploration of Metal Vanadate Thin-Film Systems (M-V-O, M = Cu, Ag, W, Cr, Co, Fe) for Solar Water Splitting: Composition, Structure, Stability, and Photoelectrochemical Properties, ACS Comb. Sci. 2020;22(12):844-857.

[13] Koo HJ, Whangbo MH, Lee KS, Investigation of the spin exchange interactions and magnetic structures of the $CrVO_4$-type transition metal phosphates, sulfates, and vanadates by spin dimer analysis, Inorg. Chem. 2003;42(19):5932-5937.

[14] Yamane H, Tanimura R, Yamada T, Takahashi J, Kajiwara T, Shimada M, Synthesis and crystal structures of $CaY_2Ge_3O_{10}$ and $CaY_2Ge_4O_{12}$, J. Solid State Chem. 2006;179(1):289-295.

[15] Mironov VS, Galyametdinov YG, Ceulemans A, Görller-Walrand C, Binnemans K, Room-temperature magnetic anisotropy of lanthanide complexes: A model study for various coordination polyhedra, J. Chem. Phys. 20021;16(11):4673-4685.

[16] Singh P, Brandenburg BJ, Sebastian CP, Singh P, Singh S, Kumar D, Parkash O, Electronic structure, electrical and dielectric properties of $BaSnO_3$ below 300 K, Jpn. J. Appl. Phys. 2008;47(5R):3540.

[17] Liu LJ, Huang YM, Su CX, Fang L, Wu MX, Hu CZ, Fan HQ, Space-charge relaxation and electrical conduction in $K_{0.5}Na_{0.5}NbO_3$ at high temperatures, Appl. Phys. A 2011;104(4):1047.

[18] Aquilanti V, Mundim KC, Elango M, Kleijn S, Kasai T, Temperature dependence of chemical and biophysical rate processes: Phenomenological approach to deviations from Arrhenius law, Chem. Phys. Lett. 2010;498(1-3):209-213.

[19] Maslov M, Openov L, Podlivaev A, On the vineyard formula for the pre-exponential factor in the Arrhenius law, Phys. Solid State 2014;56(6):1239-1244.

[20] Zhang L, Chen XM, Dielectric relaxation in $LuFeO_3$ ceramics, Solid State Commun. 2009;149(33-34):1317-1321.

[21] Lupascu DC, Genenko YA, Balke N, Aging in ferroelectrics, J. Am. Ceram. Soc. 2006;89(1):224-229.

[22] Rahmani M, Pithan C, Waser R, Electric transport properties of rare earth doped $Yb_xCa_{1-x}MnO_3$ ceramics (part II: The role of grain boundaries and oxygen vacancies), J. Eur. Ceram. Soc. 2019;39(15):4800-4805.

[23] Scott MG, Kuršumović A, Short-range ordering during structural relaxation of the metallic glass $Fe_{40}Ni_{40}B_{20}$, Acta Metall. Mater. 1982;30(4):853-860.

[24] Mauritz KA, Dielectric relaxation studies of ion motions in electrolyte-containing perfluorosulfonate ionomers. 4. Long-range ion transport, Macromol. 1989;22(12):4483-4488.

[25] D. Maslov, Y. Levinson, S. Badalian, Interedge relaxation in a magnetic field, Physical Review B 1992;46(11):7002.

[26] Tai LW, Nasrallah MM, Anderson HU, Sparlin DM, Sehlin SR, Structure and electrical properties of $La_{1-x}Sr_xCo_{1-y}FeyO_3$. Part 2. The system $La_{1-x}Sr_xCo_{0.2}Fe_{0.8}O_3$, Solid State Ionics 1995;76(3-4):273-283.

[27] Zhang BW, Li LX, Luo WJ, Oxygen vacancy regulation and its high frequency response mechanism in microwave ceramics, J. Mater. Chem. C 2018;6(41):11023-11034.

Table 1 Wyckoff positions, displacement parameters and refinement factors for $Na_2SrV_4O_{12}$.

Atoms	Wyckoff positions	*x*	*y*	*z*	Occ.	Biso.
Sr	2 b	0.2500	0.2500	0.2500	0.2500	0.151
O2	16 n	0.1839	0.0529	0.2352	1.0000	1.242
O1	16 n	0.6305	0.3695	0.1553	1.0000	0.482
V	8 k	0.5353	0.2500	0.0000	0.2500	0.702
Na	4 f	0.0000	0.0000	0.5000	0.0625	0.500
Lattice parameter			a = 10.6345	b = 10.6345	c = 4.9621	
Crystal system				*Tetragonal*		
Space group				*P4/nbm*		
$R_p/R_{wp}/\chi^2$			R_{wp} =	R_p = 4.46%	χ^2 = 2.13	

6.87%

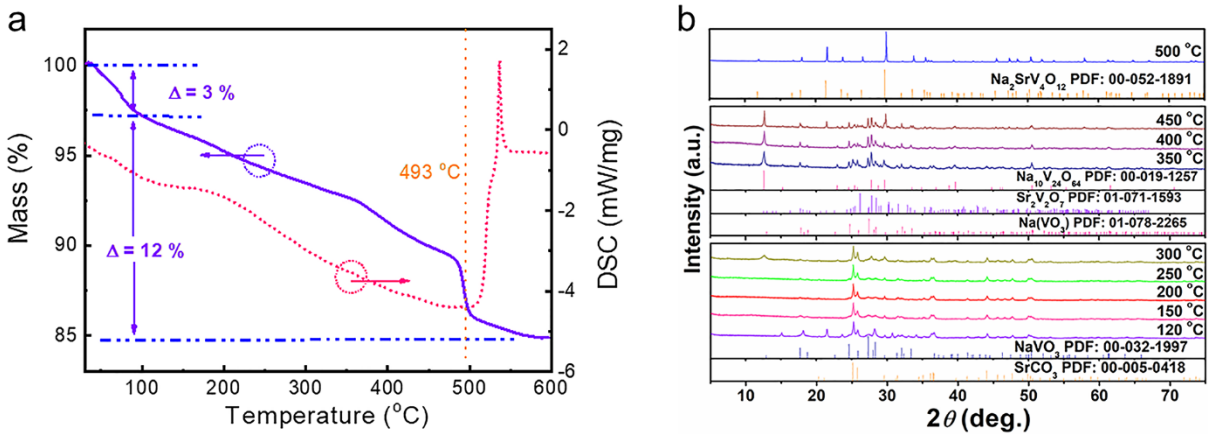

Fig. 1 a Thermal analysis of the mixed raw materials of $Na_2SrV_4O_{12}$ before calcination; **b** XRD patterns of $Na_2SrV_4O_{12}$ ceramics sintered at various temperatures (120- 500 °C).

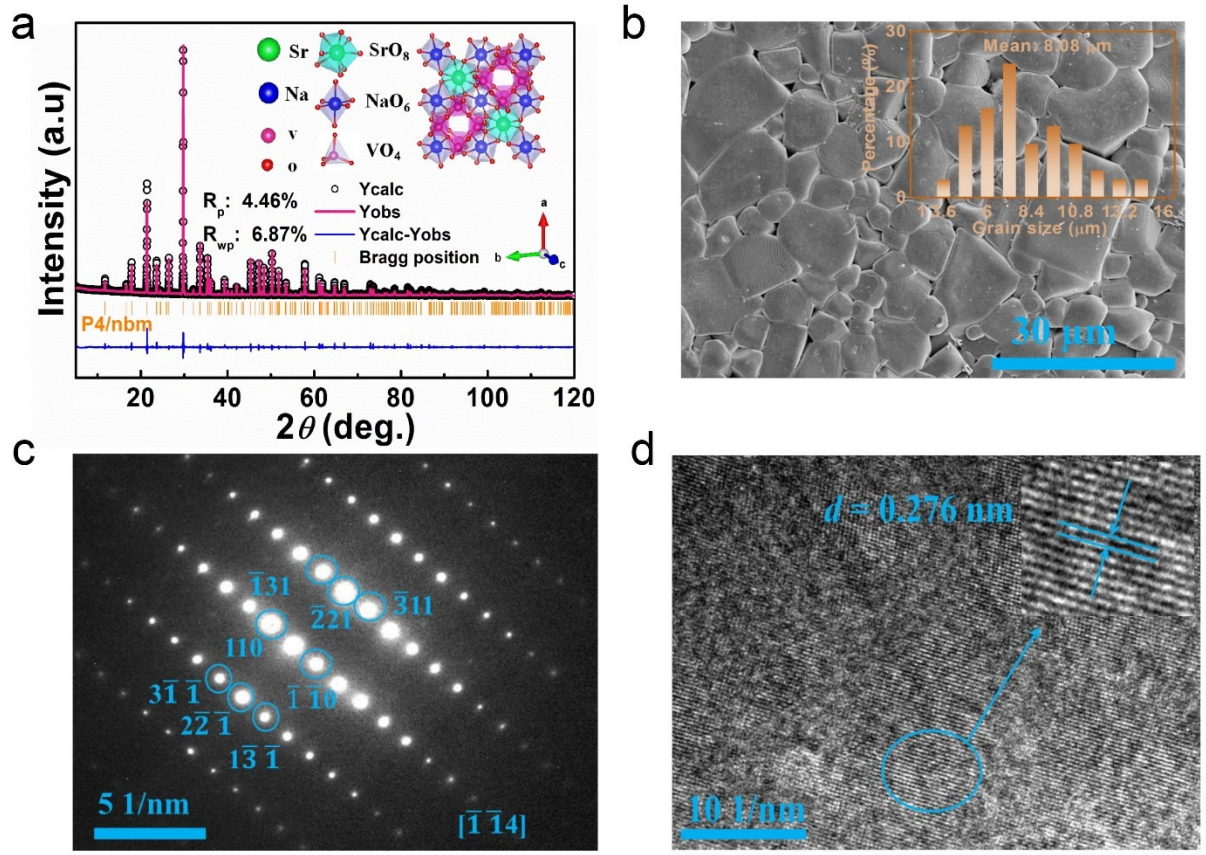

Fig. 2 a A representative Rietveld refinement plots for the cracked $Na_2SrV_4O_{12}$ powders sintered at 550 °C/4h (crystal structure showing the coordination polyhedra of Sr^{2+}, Na^{+}, and V^{5+} is shown in the inset); **b** SEM image on the surface of the ceramic sintered at 550 °C/4h with the grain size distribution; **c** selected area electron diffraction patterns with a $[\bar{1}\bar{1}4]$ zone axis; **d** HRTEM image of the $Na_2SrV_4O_{12}$.

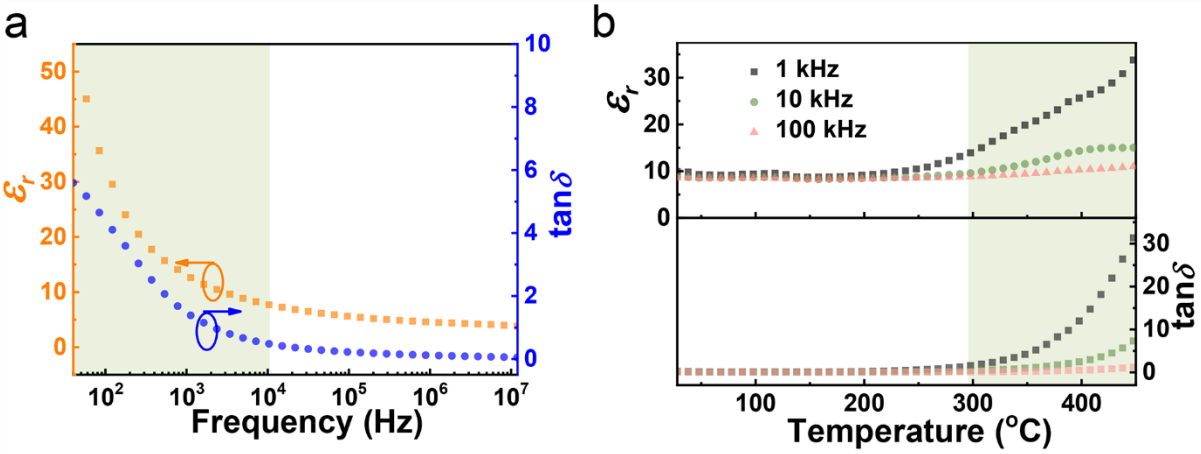

Fig. 3 Frequency (**a**, in a range of 10-10^7 Hz) and temperature (b, in a range of 25-450 °C) dependence of dielectric properties.

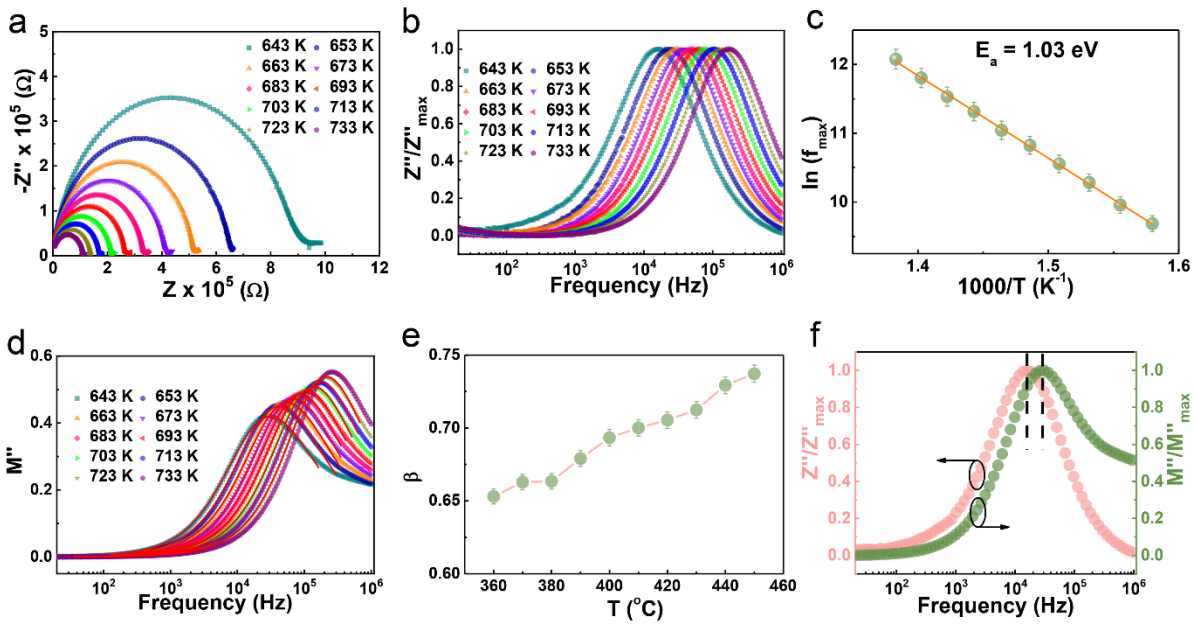

Fig. 4 a Complex impedance plots at various temperatures (643-733 K); **b** the frequency dependence of the normalized imaginary part of impedance (Z'') at the same temperature range; **c** the Arrhenius plot for the relaxation frequency as shown in Fig. 4b; **d** the frequency dependence of the imaginary part of modulus (M'') at various temperatures (643-733 K); **e** the degree of deviation from the ideal Debye relaxation (β) as a function of temperature; **f** the normalized Z''/Z''_{max} and M''/M''_{max} at 653 K.

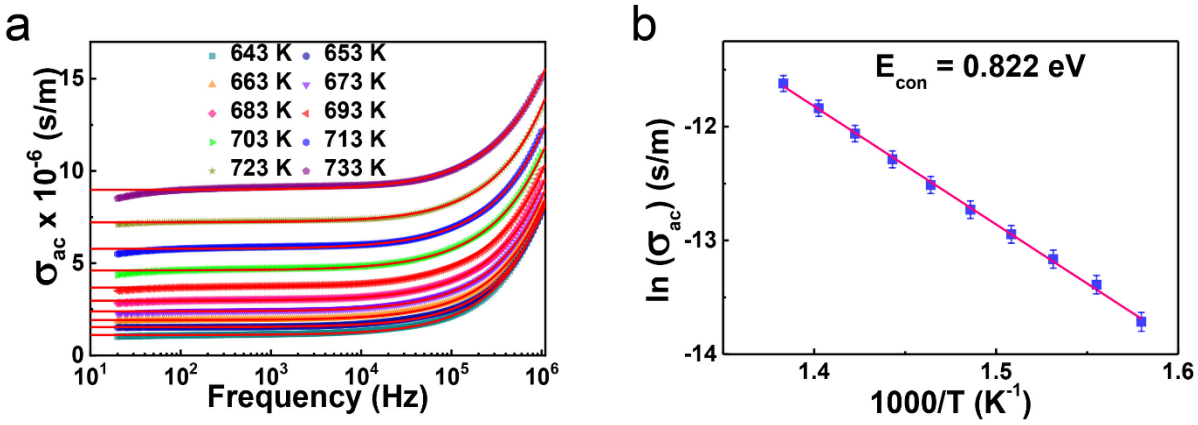

Fig. 5 a the frequency dependence of ac conductivity at various temperatures (643-733 K); **b** the Arrhenius plot for the conductivity.

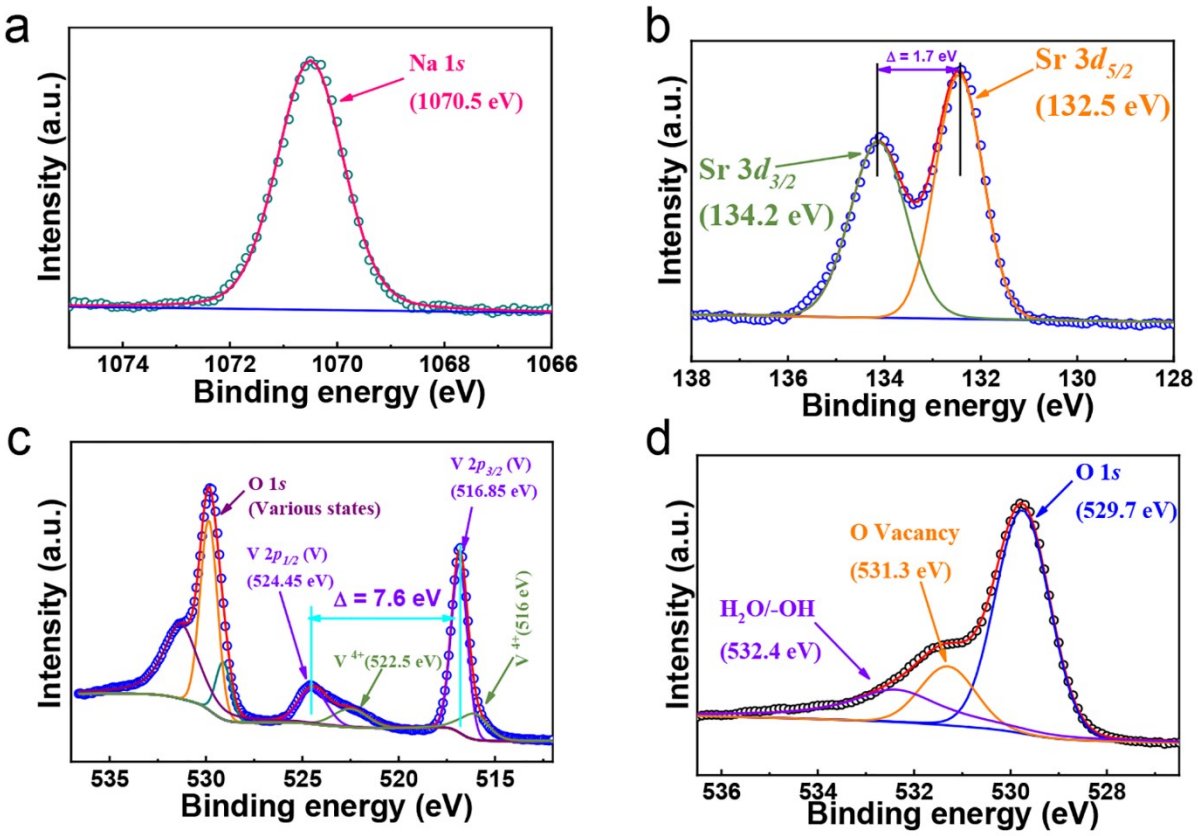

Fig. 6 a-d XPS curves for Na, Sr, V, and O elements.